photonics

MDPI

Article

Extended Operational Ghost Correlation Model: Ghost Arithmetic Operations for Multi-Channel Information Synthesis

Jilun Zhao and Haibo Wang *

Applied Optics Beijing Area Major Laboratory, School of Physics and Astronomy, Beijing Normal University, Beijing 100875, China

* Correspondence: hbwang@bnu.edu.cn

Abstract

Ghost imaging, ghost interference, and ghost diffraction retrieve an object's spatial distribution and interference–diffraction patterns via intensity correlation. Flexibly synthesizing multi-channel optical information within a single correlation architecture is a key challenge in the evolution of optical correlation from fundamental research to information processing platforms. This study proposes the Extended Operational Ghost Correlation Model (EO-GCM), which introduces the four arithmetic operations (addition, subtraction, multiplication, and division) into optical correlation data processing. Within circular complex Gaussian pseudothermal light fields, the study systematically derives the analytical expressions for the second-order intensity fluctuation correlations with these operations. The theory shows that addition and subtraction obey superposition, whereas for multiplication and division, the average intensity of one object path becomes a weighting factor for the information of the other path. When weakly correlated, multiplication yields a weighted sum, whereas division yields a weighted difference, with the two weights having opposite signs. Experiments on ghost interference or diffraction and ghost imaging verify theoretical predictions and confirm the proportionality between the absolute value of the negative weight in division and the average intensity of the numerator path. The proposed model enables basic operations on multipath object signals, endowing optical correlation systems with reconfigurable, weighted correlation fusion-based information modulation capabilities.

Keywords: ghost imaging; ghost interference; second-order correlation; arithmetic operations; weight manipulation

1. Introduction

In 1956, the Hanbury Brown–Twiss intensity interference experiment was designed to measure the angular diameter of stars, revealing for the first time the statistical correlation properties of intensity fluctuations in light fields and thereby laying the experimental foundation for the study of second-order coherence of light [1]. In the 1960s, Glauber [2] established the quantum statistical mechanics framework for optical coherence, providing a complete quantum explanation for the HBT experimental results. Based on this theory, in 1995, Strekalov et al. [3] first realized nonlocal double-slit interference using entangled photon pairs. This experiment is known as the ghost interference experiment. In the same year, Pittman et al. [4] demonstrated nonlocal imaging using entangled light sources, i.e., the ghost imaging experiment.

Check for updates

Received: 15 February 2026
Revised: 4 May 2026
Accepted: 28 May 2026
Published: 8 June 2026

Copyright: © 2026 by the authors. Licensee MDPI, Basel, Switzerland. This article is an open access article distributed under the terms and conditions of the Creative Commons Attribution (CC BY) license.

Since then, the study of second-order coherence has become an important approach to revealing the nature of light, leading to the discovery of novel second-order interference phenomena. From 2002 onward, research showed that classical light sources with intensity fluctuations, typically thermal light, can also realize ghost imaging and ghost interference [5–22]. This conclusion extended ghost effects from the quantum domain to the classical domain, prompting a systematic examination of the intrinsic relationship between the first-order and second-order coherence of light [9,23]. To date, techniques based on second-order coherence have been widely applied in various fields, including turbulence-free imaging [24,25], adaptive optics [26,27], and optical classification [28,29], demonstrating broad application prospects. However, as research progresses, demands such as the parallel detection of multiple object beams [30–32] and multi-modal information fusion [33] are increasingly prominent. Recently, deep learning has been successfully applied to ghost imaging for tasks such as learning-based reconstruction, denoising, sampling reduction, and physics-informed network-based imaging [34–41]. A key challenge is how to flexibly synthesize, compare, and selectively extract various types of information, such as spatial frequency and intensity distribution, carried by different object channels within a single correlation architecture. This issue has become central as optical correlation evolves from "imaging measurement" to "information processing," where the former refers to passively reproducing a single object's image or spectrum, while the latter signifies actively combining, weighting, and selectively extracting multi-channel data to enable advanced functionalities such as image fusion, feature comparison, and adaptive decision-making.

A natural and direct solution is to introduce the four basic arithmetic operations into the optical correlation data processing workflow, providing a straightforward and efficient path to achieve the above functions. Performing addition, subtraction, multiplication, or division on the intensity signals of multiple object beams before correlating them with the reference light is expected to transform the traditional correlation result from a "passive presentation of independent channel information" into an "active manipulation and synthesis of multi-channel information". However, existing discussions on basic operations in optical correlation are still scattered: the superposition property of linear operations (addition, subtraction) is a direct consequence of the second-order correlation formalism itself [42], whereas nonlinear operations (multiplication, division) have been applied in some experiments [21,35,43–45] and core theoretical issues such as the analytical relationship between the correlation function and the statistical properties of the light field, the weighting rules, and the sign modulation mechanism have not yet been deeply clarified.

To address these issues, this study proposes the Extended Operational Ghost Correlation Model (EO-GCM). Within the statistical framework of circular complex Gaussian pseudothermal light fields, this study systematically derives the analytical expressions for the second-order intensity fluctuation correlation functions corresponding to the four fundamental arithmetic operations (addition, subtraction, multiplication, and division). The circular complex Gaussian distribution, as the standard statistical model for thermal light fields, has a remarkably wide range of applicability, capable of describing the statistical behavior of thermal light sources both in nature and across various application scenarios. This framework is adopted in the present study to accommodate such diverse application scenarios. The model fully retains the contributions of inter-object mutual correlation and the three-field interference term, making it applicable to arbitrary correlation scenarios. Furthermore, by introducing the typical condition of weak object correlation, the study clearly reveals the essence of weight manipulation by nonlinear operations on correlation signals. Specifically, multiplication converts the average intensity of one object beam into a positive weight for the information of the other object beam, achieving linear amplification of the target information. Conversely, division endows it with a negative weight, whose absolute

value is proportional to the average intensity of the numerator object beam, thereby realizing sign-adjustable weighted subtraction. This discovery transforms nonlinear operations into a physical degree of freedom for information weighting, endowing ghost imaging systems with novel capabilities of dynamic weighting and sign-adjustable processing.

To verify the theoretical predictions, two types of experiments were designed and conducted: one based on ghost interference or diffraction, intended to verify the correlation after arithmetic preprocessing behavior for spatial frequency information, and the other based on ghost imaging, intended to verify the correlation after arithmetic preprocessing behavior for intensity distribution information. Both sets of experiments were conducted under the condition of weak object correlation, and the measurement results were in quantitative agreement with the theoretical model. By systematically tuning the average intensity of one object beam, the experiments directly demonstrated the continuous and linear manipulation capability of multiplication and division on the contribution proportion of information from the other beam. For the first time, these experiments confirmed that the absolute value of the negative weight in division is proportional to the average intensity of the numerator beam.

The remainder of this paper is organized as follows: Section 2 discusses the theoretical framework of EO-GCM, sequentially deriving the correlation expressions for linear and nonlinear operations and providing simplified forms under the weak correlation condition. Section 3 presents the experimental setup, parameter settings, and data processing methods, reports the experimental results for both ghost interference or diffraction and ghost imaging configurations, and demonstrates the quantitative verification of the weight manipulation mechanism. Section 4 discusses the extension of the theoretical model to cases with finite object correlation. Finally, Section 5 concludes the paper and provides an outlook on the application prospects of this framework in fields such as adaptive imaging, multiparameter detection, and all-optical information processing.

2. Theoretical Model

The schematic diagram of the EO-GCM framework is shown in Figure 1. The pseudothermal light source is first split into two beams. One beam passes through a reference system and is received by a detector, called the reference arm. The other beam is split again, passing through test system 1 containing object 1 and test system 2 containing object 2, before being received by detectors. The corresponding optical signals are called object arm 1 and object arm 2. The three intensity signals are measured synchronously. In this model, the four basic arithmetic operations are performed on the intensity signals of object arm 1 and object arm 2, and the result is then correlated with the reference arm signal via intensity fluctuation correlation.

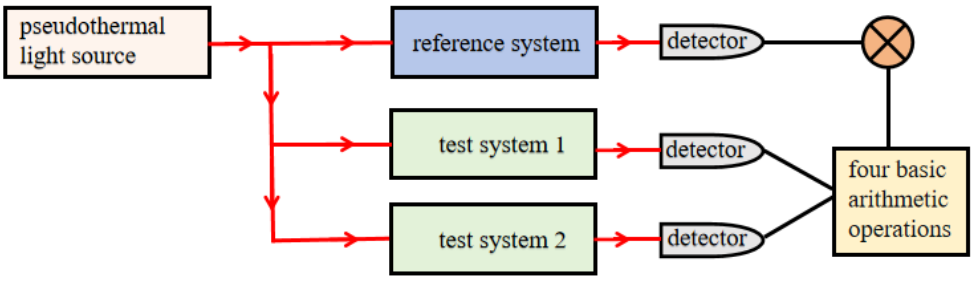


Figure 1. Schematic diagram of the EO-GCM.

Let the intensity of the reference arm be I_R and the intensities of object arm 1 and object arm 2 be I_{O1} and I_{O2}, respectively. In the theoretical framework of this paper, I_{O1} and I_{O2} generally refer to the intensity signals of the object arm, whose specific form

depends on the experimental configuration. In point-detection experiments, such as ghost interference or diffraction, they represent the intensity at a single point. In bucket-detection experiments, such as ghost imaging, they represent the total intensity collected by the detector (i.e., the intensity integrated over the effective area). All correlation functions are defined and derived based on the statistics of intensity fluctuations, independent of the detection scheme. Therefore, the conclusions can be uniformly applied to both types of experiments. The result after data processing in this model can be expressed as follows:

$$\begin{aligned} \Delta G^{(2)}_{R,(O1\circ O2)} &= \langle \Delta I_R \cdot \Delta(I_{O1} \circ I_{O2}) \rangle \\ &= \langle I_R (I_{O1} \circ I_{O2}) \rangle - \langle I_R \rangle \langle I_{O1} \circ I_{O2} \rangle \end{aligned} \tag{1}$$

where the symbol "$\circ$" represents one of the four fundamental arithmetic operations applied to I_{O1} and I_{O2}, and $\Delta G^{(2)}_{R,(O1\circ O2)}$ denotes the second-order intensity fluctuation correlation between the reference arm and the result of the operation.

The correlation results under the four fundamental arithmetic operations will be discussed separately below. First, for linear operations, using the Gaussian statistical properties of the pseudothermal light field and the Gaussian moment theorem [42], Equation (1) can be specifically derived as follows:

$$\begin{aligned} \Delta G^{(2)}_{R,(O1\pm O2)} &= \langle I_R (I_{O1} \pm I_{O2}) \rangle - \langle I_R \rangle \langle I_{O1} \pm I_{O2} \rangle \\ &= \Delta G^{(2)}_{R,O1} \pm \Delta G^{(2)}_{R,O2}. \end{aligned} \tag{2}$$

Here, $\Delta G^{(2)}_{R,O1} = \langle I_R I_{O1} \rangle - \langle I_R \rangle \langle I_{O1} \rangle$ and $\Delta G^{(2)}_{R,O2} = \langle I_R I_{O2} \rangle - \langle I_R \rangle \langle I_{O2} \rangle$ represent the second-order intensity fluctuation correlation functions between the reference light and object arms 1 and 2, respectively. Equation (2) indicates that for linear operations, the final correlation result is equivalent to the linear superposition of the second-order intensity correlations between the two object beams and the reference arm. This allows direct separation or comparison of the contributions of the two objects to the correlation signal. Since both correlation signals contribute positively, the total signal is their sum, and the proportion of each information channel is entirely predetermined by the object's own correlation strength with the reference arm.

However, when the operation is multiplication or division, the nonlinearity introduces richer higher-order statistical correlations [16,35,46–48]. For systematic analysis, we first consider the multiplication operation, whose correlation function is as follows:

$$\Delta G^{(2)}_{R,(O1\times O2)} = \langle I_R (I_{O1} \times I_{O2}) \rangle - \langle I_R \rangle \langle I_{O1} \times I_{O2} \rangle. \tag{3}$$

For Equation (3), we can rewrite it in the form of a sixth-order moment of the fields:

$$\Delta G^{(2)}_{R,(O1\times O2)} = \langle U_R U_R^* U_{O1} U_{O1}^* U_{O2} U_{O2}^* \rangle - \langle U_R U_R^* \rangle \langle U_{O1} U_{O1}^* U_{O2} U_{O2}^* \rangle. \tag{4}$$

According to the Gaussian moment theorem, for six complex random variables $z_1, z_2, z_3, z_4, z_5, z_6$ that obey a joint Gaussian distribution, we have: $\langle z_1 z_2 z_3 z_4 z_5 z_6 \rangle = \sum_{\text{all pairings}} \langle z_i z_j \rangle \langle z_k z_l \rangle \langle z_m z_n \rangle$. Applying this result to Equation (4) and taking into account that for actual light fields $\langle U^k \rangle = 0$, Equation (3) can be further explicitly expressed as:

$$\begin{aligned} \Delta G^{(2)}_{R,(O1\times O2)} = \langle I_{O2} \rangle \Delta G^{(2)}_{R,O1} + \langle I_{O1} \rangle \Delta G^{(2)}_{R,O2} + \langle I_R \rangle \Delta G^{(2)}_{O1,O2} \\ + 2\,\mathrm{Re}\left\{ G^{(1)}_{R,O1} G^{(1)}_{O1,O2} G^{(1)*}_{R,O2} \right\}, \end{aligned} \tag{5}$$

where $G^{(1)}_{R,O1} = \langle U_R U^*_{O1} \rangle$, $G^{(1)}_{R,O2} = \langle U_R U^*_{O2} \rangle$, and $G^{(1)}_{O1,O2} = \langle U_{O1} U^*_{O2} \rangle$ are the first-order correlation functions, and $\Delta G^{(2)}_{O1,O2} = \langle I_{O1} I_{O2} \rangle - \langle I_{O1} \rangle \langle I_{O2} \rangle$ is the intensity fluctuation correlation between the two object beams. Equation (5) shows that the multiplication correlation result consists of three parts, including a weighted sum of two independent correlations, $\langle I_{O2} \rangle \Delta G^{(2)}_{R,O1} + \langle I_{O1} \rangle \Delta G^{(2)}_{R,O2}$, with the weights being the average intensities of the other path; the inter-object mutual correlation term $\langle I_R \rangle \Delta G^{(2)}_{O1,O2}$; and the three-field interference term $2\,\mathrm{Re}\{G^{(1)}_{R,O1} G^{(1)}_{O1,O2} G^{(1)*}_{R,O2}\}$. Note that for point detection, $\Delta G^{(2)}_{R,O1}$ coincides with $|G^{(1)}_{R,O1}|^2$; for bucket detection (as in ghost imaging), $\Delta G^{(2)}_{R,O1}$ naturally takes an integral form $\int |G^{(1)}_{R,O1}(\boldsymbol{\rho})|^2 d\boldsymbol{\rho}$. Therefore, the expressions remain valid for both detection schemes.

Next, we consider the division operation, whose correlation function is as follows:

$$\Delta G^{(2)}_{R,(O1/O2)} = \langle I_R (I_{O1}/I_{O2}) \rangle - \langle I_R \rangle \langle I_{O1}/I_{O2} \rangle. \tag{6}$$

Because of the stronger nonlinearity of division, its analytical treatment is more complex than multiplication. A direct mathematical understanding is that this correlation quantity measures the statistical correlation between the reference arm intensity I_R and the intensity ratio I_{O1}/I_{O2} of the two object beams. For pseudothermal light fields obeying circular complex Gaussian statistics, to obtain an analytical expression for the correlation signal, we use the Taylor expansion method for $1/I_{O2}$.

$$\frac{1}{I_{O2}} = \frac{1}{\langle I_{O2} \rangle + \delta I_{O2}} = \frac{1}{\langle I_{O2} \rangle} \sum_{n=0}^{\infty} (-1)^n \left(\frac{\delta I_{O2}}{\langle I_{O2} \rangle} \right)^n, \tag{7}$$

where $\delta I_{O2} = I_{O2} - \langle I_{O2} \rangle$ (which is numerically the same as ΔI used in the definition of correlation functions). The δ symbol is used here to emphasize its role as a small perturbation parameter in the Taylor expansion, satisfying the convergence condition $|\delta I_{O2}|/\langle I_{O2} \rangle < 1$. For actual pseudothermal light, the relative amplitude of intensity fluctuations $|\delta I_{O2}|/\langle I_{O2} \rangle$ is usually less than 1. In this case, the Taylor series expressed in Equation (7) has good pointwise convergence, and retaining terms up to second order ($n \leq 2$) provides a sufficiently accurate approximate description of the division correlation. The truncation error of this expansion is dominated by the first neglected term, which is of order $(\delta I_{O2}/\langle I_{O2} \rangle)^3$. Under typical experimental conditions, the relative intensity fluctuation satisfies $|\delta I_{O2}|/\langle I_{O2} \rangle \sim 0.5$, yielding a relative error of approximately $(0.5)^3 = 12.5\%$. This level of accuracy is sufficient for the weak correlation regime considered in this study. It is worth noting that when the average intensity $\langle I_{O2} \rangle$ is low, the relative fluctuation amplitude $|\delta I_{O2}|/\langle I_{O2} \rangle$ can become large, which degrades the accuracy of the truncated Taylor expansion. In such cases, higher-order terms in the expansion should be retained to ensure convergence. Substituting Equation (7) truncated to second order into the correlation function yields the following approximate expression for the division correlation function:

$$\begin{aligned} \Delta G^{(2)}_{R,(O1/O2)} \approx & \frac{1}{\langle I_{O2} \rangle} \Delta G^{(2)}_{R,O1} - \frac{\langle I_{O1} \rangle}{\langle I_{O2} \rangle^2} \Delta G^{(2)}_{R,O2} \\ & - \frac{2}{\langle I_{O2} \rangle^2} \mathrm{Re}\left\{ G^{(1)}_{R,O1} G^{(1)}_{O1,O2} G^{(1)*}_{R,O2} \right\} \\ & + \frac{1}{\langle I_{O2} \rangle^3} \left[\langle I_R I_{O1} (\delta I_{O2})^2 \rangle - \langle I_R \rangle \langle I_{O1} (\delta I_{O2})^2 \rangle \right]. \end{aligned} \tag{8}$$

The same interpretation of $\Delta G^{(2)}$ for point and bucket detection applies here. Equation (8) shows that the division correlation also comprises three parts: a weighted sum of two inde-

pendent correlations (with weights $1/\langle I_{O2}\rangle$ and $-\langle I_{O1}\rangle/\langle I_{O2}\rangle^2$), the three-field interference term, and higher-order terms involving $(\delta I_{O2})^2$.

Since these general expressions can be greatly simplified when the inter-object correlation is weak, we will focus on this practically important case. In specific applications and experiments, making the correlation between object arms sufficiently weak (e.g., by beam splitting with beam splitters or illumination by independent sources) can ensure the Gaussian statistical properties of the pseudothermal light field while effectively suppressing the interference from inter-object mutual correlation and the three-field interference term. This provides a reasonable starting point for testing theoretical predictions and calibrating system parameters. At the theoretical level, the weak correlation assumption also constitutes a necessary path for analytical derivation. When the correlation between object arms is negligible, the inter-object mutual correlation term and the three-field interference term in multiplication automatically tend to zero. In division, the cross-moments involving $\langle I_R I_{O1}\delta I_{O2}\rangle$ and $\langle I_R I_{O1}(\delta I_{O2})^2\rangle$ are also significantly simplified due to the approximate independence of intensity fluctuations. The correlation expressions for both nonlinear operations are reduced to quasi-linear weighted forms dominated solely by $\Delta G^{(2)}_{R,O1}$ and $\Delta G^{(2)}_{R,O2}$ and their corresponding light intensity weights, thereby stripping away the complex influences of higher-order coherent coupling and revealing the weight assignment rules and sign modulation capabilities inherent to the nonlinear operations themselves. To provide a measurable criterion for weak correlation, we introduce the normalized second-order correlation function $g^{(2)}_{O1,O2} = \langle I_{O1}I_{O2}\rangle/(\langle I_{O1}\rangle\langle I_{O2}\rangle)$. This criterion can be directly tested experimentally, where $g^{(2)}_{O1,O2} \simeq 1$ indicates statistical independence of the two object arms.

For the multiplication operation, when $\Delta G^{(2)}_{O1,O2} \simeq 0$, Equation (5) can be rewritten as follows:

$$\Delta G^{(2)}_{R,(O1\times O2)} = \langle I_{O2}\rangle \Delta G^{(2)}_{R,O1} + \langle I_{O1}\rangle \Delta G^{(2)}_{R,O2}. \tag{9}$$

Under this condition, the multiplication correlation manifests as a linear superposition form, where the weights are determined by the light intensities. In the final correlation signal, the contribution proportion of the information from each object is linearly modulated by the average intensity of the other object beam. By changing the average intensity of one object beam, one can linearly tune the contribution of the other object's information in the correlation result, and this tuning is directional, that is, it only affects the weight of the other channel's information. This provides a tuning mechanism for the selective extraction of multi-channel information. Notably, although the operation itself is nonlinear, the final correlation expression still exhibits linear superposition at the level of $\Delta G^{(2)}_{R,Oi}$, and only the superposition coefficients originate from the product of light intensities introduced by the nonlinear operation. This indicates that in optical correlation, nonlinear operations can alter the processing function of the system by changing the weighting rules for information synthesis.

Next, consider the division operation. When $\Delta G^{(2)}_{O1,O2} \simeq 0$, Equation (8) can be rearranged as follows:

$$\Delta G^{(2)}_{R,(O1/O2)} \approx \frac{1}{\langle I_{O2}\rangle^2}\left[\left(\langle I_{O2}\rangle + \frac{\sigma^2_{I_{O2}}}{\langle I_{O2}\rangle}\right)\Delta G^{(2)}_{R,O1} - \langle I_{O1}\rangle \Delta G^{(2)}_{R,O2}\right], \tag{10}$$

where $\sigma^2_{I_{O2}} = \langle \delta I^2_{O2}\rangle$ is the intensity fluctuation variance of object arm 2. Under actual experimental conditions, the statistical properties of pseudothermal light fields are usually stable, and $\sigma^2_{I_{O2}}$ can be considered a fixed parameter. Through Equation (10), the division correlation can be expressed as a linear combination of two independent correlation terms $\Delta G^{(2)}_{R,O1}$ and $\Delta G^{(2)}_{R,O2}$. The effective weight for the first term $\Delta G^{(2)}_{R,O1}$ is $\langle I_{O2}\rangle + \sigma^2_{I_{O2}}/\langle I_{O2}\rangle$,

with its main part proportional to the average intensity $\langle I_{O2} \rangle$ of the denominator object beam, while the additional variance term originates from the second-order ($n = 2$) contribution of the Taylor expansion. The weight for the second term $\Delta G^{(2)}_{R,O2}$ is $-\langle I_{O1} \rangle$, and its magnitude and sign are entirely determined by the average intensity $\langle I_{O1} \rangle$ of the numerator object beam. Therefore, the division correlation manifests as a weighted subtraction of two-channel correlation information, and the weight of each channel's information is directly related to the average intensity of the other object beam—this weight assignment rule is highly similar to that of multiplication.

In particular, under the condition of fixed $\langle I_{O2} \rangle$, the absolute value of the weight for the $\Delta G^{(2)}_{R,O2}$ term in division is proportional to $\langle I_{O1} \rangle$, which is completely consistent with the rule that the weight for the $\Delta G^{(2)}_{R,O2}$ term in multiplication increases linearly with $\langle I_{O1} \rangle$. The weight manipulation of the object arm 2 channel information in both nonlinear operations exhibits a linear proportional relationship dominated by $\langle I_{O1} \rangle$, with the core difference being that multiplication gives a positive weight while division gives a negative weight. This symmetric structure reveals a universal weight assignment mechanism for nonlinear operations in optical correlation. Regardless of whether multiplication or division is used, the average intensity of one object beam can serve as an effective tuning parameter for the contribution proportion of information from the other beam. The selectivity of the sign of this tuning endows ghost imaging systems with dynamic weighting and sign-adjustable information processing capabilities within a single architecture.

In summary, the proposed EO-GCM provides a systematic mathematical foundation for performing basic operations on multipath object arm signals within the framework of optical correlation. The model rigorously derives the universal form of linear operations (addition, subtraction) where the correlation result is the linear superposition of independent correlation signals. More importantly, through the introduction of nonlinear operations (multiplication, division), it discovers new mechanisms for correlation signal synthesis. Multiplication achieves controllable amplification of information contribution by using the average intensity of one object beam as the weight for the other object's correlation signal; division, by coupling the intensity ratio, statistical fluctuations, and intensity signal mutual correlation, enables the correlation signal to continuously transition between weighted difference and weighted sum. These findings reveal how operational nonlinearity can be transformed into a physical degree of freedom for information manipulation, laying a theoretical foundation for achieving fusion, comparison, and selective extraction of multi-channel information in correlation measurements. The dynamic weighting and sign-adjustable capabilities realized based on this framework allow ghost imaging systems to continuously tune target features within a single architecture, providing reconfigurable, electro-optic modulation-free technical pathways for fields such as adaptive imaging, multiparameter joint detection, and all-optical information processing.

3. Experiments

In optical correlation experiments, the object arm typically contains either the spatial frequency information or the intensity distribution information of the object. To systematically test the theoretical predictions of the EO-GCM theory for the correlation of these two types of information under the condition of weak object correlation, we designed two types of experiments: one based on ghost interference or diffraction to verify the spatial frequency correlation described by the theory, and the other based on ghost imaging to verify the intensity distribution correlation described by the theory.

First, to verify the case where the object arm carries the spatial frequency information of the object, we built the experimental optical path shown in Figure 2(a1). The light source is a He-Ne laser ($\lambda = 632.8$ nm). Its output beam is first polarization-adjusted by

a polarizer P and a half-wave plate H, and is then incident on a reflective spatial light modulator SLM loaded with a random phase to generate pseudothermal light. This light passes through two convex lenses L_1 and L_2 and is then split into two beams by the beam splitter BS_1. One beam propagates freely and is received by a CMOS image sensor CIS_R to record the intensity information as the reference path. The other beam is further split by beam splitter BS_2 into two paths, passing through objects O_{IN1} and O_{IN2}, respectively, and is then received by CIS_1 and CIS_2 to record the intensity information. In this experiment, we denote the signal recorded by CIS_R as the reference arm (I_R), the signal passing through O_{IN1} and received by CIS_1 as object arm 1 (I_{O1}), and the signal passing through O_{IN2} and received by CIS_2 as object arm 2 (I_{O2}). Lenses L_1 (focal length 200 mm) and L_2 (focal length 75 mm) are placed confocally (i.e., the back focal plane of L_1 coincides with the front focal plane of L_2), forming a beam transformation system whose main function is to reduce the transverse coherence length of the pseudothermal light generated by the SLM modulation. The distances from BS_1 to all three CISs are 800 mm. Objects O_{IN1} and O_{IN2} are at distances $z = 600$ mm from CIS_1 and CIS_2, respectively. The experimental configuration where object arms 1 and 2 are individually correlated with the reference arm can be considered a ghost interference or diffraction experiment. The SLM used in the experiment is Holoeye VIS-016 (1080 × 1920 pixels, pixel pitch 8 µm, Holoeye, Berlin, Germany), and the CIS is MER-231-41U3M (1920 × 1200 pixels, Daheng, Beijing, China).

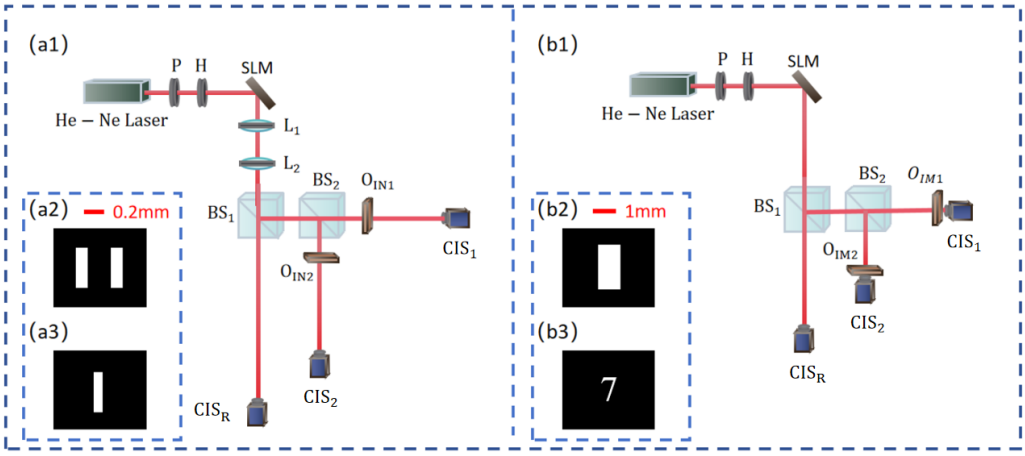


Figure 2. EO-GCM experimental setup. (**a**) Spatial frequency correlation experimental configuration (ghost interference or diffraction). (**a1**) Experimental optical path diagram: P: polarizer; H: half-wave plate; SLM: reflective spatial light modulator loaded with a random phase; L_1, L_2: confocal lens system; BS_1, BS_2: beam splitters; CIS_R: reference path detector; CIS_1, CIS_2: object path detectors; O_{IN1}: double slit; O_{IN2}: single slit. (**a2**) Schematic diagram of the double slit O_{IN1}. (**a3**) Schematic diagram of the single slit O_{IN2}. (**b**) Spatial distribution correlation experimental configuration (ghost imaging). (**b1**) Experimental optical path diagram, except that the objects are replaced by O_{IM1} (transmissive rectangle) and O_{IM2} (transmissive digit "7"); all other optical components and parameters are the same as in (**a1**). (**b2**) Schematic diagram of the rectangle O_{IM1}. (**b3**) Schematic diagram of the digit "7" O_{IM2}. The three intensity signals are acquired synchronously and subjected to correlation after arithmetic preprocessing analysis.

In the above experiments, the three intensity signals I_R, I_{O1}, I_{O2} are acquired synchronously with a sampling frequency of 5 Hz. For each measurement, $N = 5000$ frames are continuously collected for subsequent statistical averaging. The reference signal $I_R(x_R)$ is taken as the one-dimensional intensity distribution along the x-direction at $y = 0$ recorded by CIS_R. The two object arm signals I_{O1} and I_{O2} are taken from the intensity at the single spatial point $(x = 0, y = 0)$ recorded by CIS_1 and CIS_2, respectively.

Schematic diagrams of objects O_{IN1} and O_{IN2} are shown in Figure 2(a2,a3). O_{IN1} is a double slit with slit width $\alpha_1 = 150$ μm and slit separation $d = 300$ μm. O_{IN2} is a single slit with slit width $\alpha_2 = 100$ μm. Their transmission functions can be expressed as follows:

$$T_{1IN}(x) = \mathrm{rect}\left(\frac{x + d/2}{\alpha_1}\right) + \mathrm{rect}\left(\frac{x - d/2}{\alpha_1}\right), \quad T_{2IN}(x) = \mathrm{rect}\left(\frac{x}{\alpha_2}\right),$$

where the rectangle function $\mathrm{rect}(x)$ is defined as $\mathrm{rect}(x) = 1$ for $|x| \leq 1/2$ and 0 otherwise. Their corresponding spatial frequency spectra $\tilde{T}_1(\xi)$ and $\tilde{T}_2(\xi)$ can be expressed as follows:

$$\tilde{T}_1(\xi) = 2\alpha_1 \,\mathrm{sinc}(\alpha_1 \xi)\cos(\pi d \xi), \quad \tilde{T}_2(\xi) = \alpha_2 \,\mathrm{sinc}(\alpha_2 \xi),$$

where $\mathrm{sinc}(x) = \sin(\pi x)/(\pi x)$, and ξ is the spatial frequency. According to the above experimental conditions, in the ghost interference or diffraction configuration, the intensity fluctuation correlations between the reference arm and the two object arms (object arms 1 and 2) are as follows:

$$\Delta G^{(2)}_{R,O1}(x_R) \propto \left|\tilde{T}_{1IN}\left(\frac{x_R}{\lambda z}\right)\right|^2 = \left|2\alpha_1 \,\mathrm{sinc}\left(\frac{\alpha_1 x_R}{\lambda z}\right)\cos\left(\frac{\pi d x_R}{\lambda z}\right)\right|^2, \tag{11}$$

$$\Delta G^{(2)}_{R,O2}(x_R) \propto \left|\tilde{T}_{2IN}\left(\frac{x_R}{\lambda z}\right)\right|^2 = \left|\alpha_2 \,\mathrm{sinc}\left(\frac{\alpha_2 x_R}{\lambda z}\right)\right|^2. \tag{12}$$

The intensity fluctuation correlation between the two object arms is proportional to the mutual overlap integral of their transmission functions, as follows:

$$\Delta G^{(2)}_{O1,O2} \propto \left|\int T_{1IN}(\rho) T^*_{2IN}(\rho)\, \mathrm{d}\rho\right|^2. \tag{13}$$

Since the spatial structures of the double slit T_{1IN} and the single slit T_{2IN} are noncoherently superposed, their mutual overlap integral is approximately zero. This result indicates that by calculating the second-order correlation of intensity fluctuations between the reference arm and each object arm separately, the spatial frequency information of the corresponding object can be retrieved, and the intensity fluctuation correlation between the two object arms approaches zero, satisfying the weak correlation condition required by the theoretical model.

The experimental results of the above experiments are shown in Figure 3. The measured correlation curves $\Delta G^{(2)}_{R,O1}(x_R)$ and $\Delta G^{(2)}_{R,O2}(x_R)$ are shown in Figure 3a,b, respectively. Their spatial frequency distributions are consistent with the theoretical expectations of Equations (11) and (12). The correlation curves of $\Delta G^{(2)}_{R,O1}$ and $\Delta G^{(2)}_{R,O2}$ clearly exhibit the modulated double-slit interference fringes and the typical single-slit diffraction envelope, respectively. This result confirms that the experimental system can effectively acquire the spatial frequency information of the objects, providing a basis for subsequent verification of correlations after arithmetic preprocessing.

Figure 3c,d show the correlation results after linear addition and subtraction operations, $\Delta G^{(2)}_{R,(O1+O2)}$ and $\Delta G^{(2)}_{R,(O1-O2)}$. The experimental curves approximate the theoretical expectations obtained by substituting Equations (11) and (12) into the linear superposition relation in Equation (2). The addition correlation $\Delta G^{(2)}_{R,(O1+O2)}$ exhibits features of both the double-slit interference fringes and the single-slit diffraction envelope, with an enhanced signal amplitude compared to the single-path correlations, consistent with the expectation of the linear superposition of two independent correlation signals. The subtraction correlation $\Delta G^{(2)}_{R,(O1-O2)}$ intuitively demonstrates the linear subtraction effect of the two correlation signals, with a significantly altered envelope shape. This clearly shows that under

linear operations, the final correlation output is equivalent to the linear combination of the independent correlations of each channel.

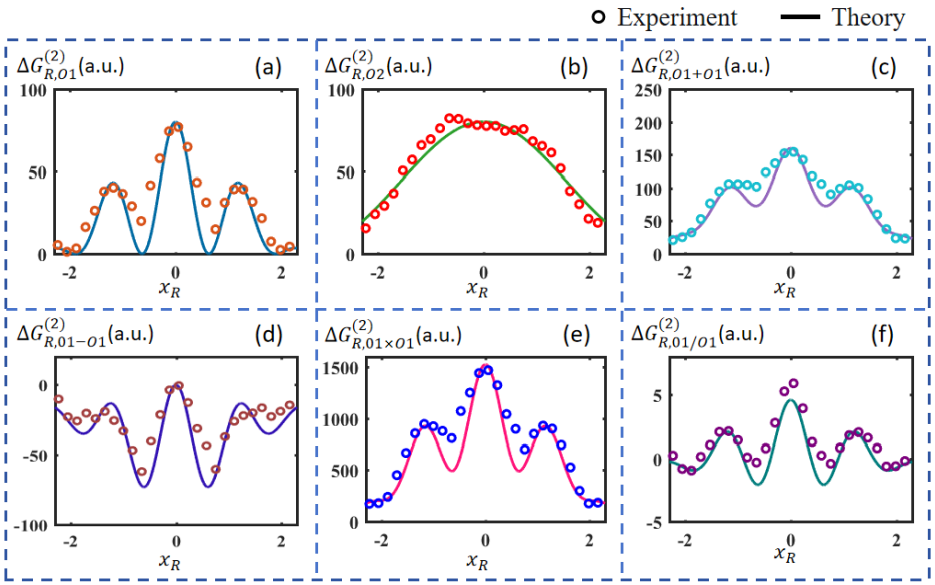


Figure 3. Theoretical and experimental results of EO-GCM under the ghost interference or diffraction configuration. (**a**,**b**) Intensity fluctuation correlations between the reference arm and single object beams: $\Delta G^{(2)}_{R,O1}$ (object arm 1), $\Delta G^{(2)}_{R,O2}$ (object arm 2); (**c**–**f**) intensity fluctuation correlation results after performing the four fundamental arithmetic operations on the two object beams and then correlating with the reference arm. (**c**) Addition $\Delta G^{(2)}_{R,(O1+O2)}$, (**d**) subtraction $\Delta G^{(2)}_{R,(O1-O2)}$, (**e**) multiplication $\Delta G^{(2)}_{R,(O1\times O2)}$, and (**f**) division $\Delta G^{(2)}_{R,(O1/O2)}$. Scatter points: experimental values; solid lines: EO-GCM theoretical curves.

For nonlinear operations, Figure 3e shows the measurement result for multiplication correlation $\Delta G^{(2)}_{R,(O1\times O2)}$. The experimental curve approximates the theoretical expectation obtained by substituting Equations (11) and (12) into the theoretical model in Equation (9). The envelope shape and amplitude of the multiplication correlation curve are similar to those of linear addition, but the weight of the double slit (corresponding to $|G^{(1)}_{R,O1}|^2$) is relatively higher. This is because the average intensity of object arm 2 ($\langle I_{O2}\rangle = 11.9$ a.u.) is higher than that of object arm 1 ($\langle I_{O1}\rangle = 6.7$ a.u.), and the mutual correlation $\Delta G^{(2)}_{O1,O2}$ between the two object arms approaches zero. This result directly verifies the conclusion of the theoretical model: under the stated conditions, the multiplication correlation manifests as a linear combination of two independent correlation signals $|G^{(1)}_{R,Oi}|^2$, with weights determined by the average intensity of the other object beam.

Figure 3f shows the measurement result for division correlation $\Delta G^{(2)}_{R,(O1/O2)}$. The experimental curve approximates the theoretical expectation obtained by substituting Equations (11) and (12) into the theoretical model in Equation (10). Similar to the subtraction operation, the division correlation also exhibits a suppressive superposition of the two correlation signals. Moreover, in division correlation, the effective weight of the first correlation signal (double slit) is jointly modulated by the denominator path intensity $\langle I_{O2}\rangle$ and its statistical fluctuations, making the influence of I_{O2} on the final correlation morphology more pronounced compared to multiplication. This result also directly validates the conclusion of the theoretical model.

To further verify its ability to carry object spatial distribution (imaging) information, we built the experimental optical path shown in Figure 2(b1). Its light source and polarization control system are the same as in the ghost interference experiment. The generated pseudothermal light field is directly incident on the beam splitter BS_1. CIS_R is placed

20 cm after BS_1 to receive the spatial intensity distribution of the reference arm. Objects O_{IM1} and O_{IM2} are placed immediately after beam splitter BS_2 in the two branches, and CIS_1 and CIS_2 are placed directly behind the two objects, respectively. Except for omitting the lens system and adjusting the detector function, the relative positions and functions of BS_1, BS_2, and the two objects are the same as in the ghost interference system. In the ghost imaging experiments, the three intensity signals were also synchronously acquired at a sampling frequency of 5 Hz for $N = 5000$ frames. The reference signal I_R is recorded by CIS_R as a two-dimensional spatially resolved intensity distribution $I_R(x_R, y_R)$. The two object arm signals I_{O1} and I_{O2} are recorded by CIS_1 and CIS_2, placed directly behind the objects, acting as bucket detectors. Schematic diagrams of objects O_{IM1} and O_{IM2} are shown in Figure 2(b2,b3),respectively. O_{IM1} is a transmissive rectangle, and O_{IM2} is a transmissive digit "7". In relative coordinates, the transmissive area of object O_{IM2} (digit "7") lies entirely within the transmissive area of object O_{IM1} (rectangle). Let the transmission functions of objects O_{IM1} and O_{IM2} be $T_{1IM}(x, y)$ and $T_{2IM}(x, y)$, respectively. Under the ghost imaging experimental system, the intensity fluctuation correlations between the two object arms and the reference arm can be expressed as follows:

$$\Delta G^{(2)}_{R,O1}(x_R, y_R) \propto |T_{1IM}(x_R, y_R)|^2, \tag{14}$$

$$\Delta G^{(2)}_{R,O2}(x_R, y_R) \propto |T_{2IM}(x_R, y_R)|^2, \tag{15}$$

The correlation between the two object arms $\Delta G^{(2)}_{O1,O2}$ is determined by the mutual overlap integral of their transmission functions:

$$\Delta G^{(2)}_{O1,O2} \propto \left| \int T_{1IM}(\vec{\rho})\, T^*_{2IM}(\vec{\rho})\, \mathrm{d}^2\vec{\rho} \right|^2, \tag{16}$$

Under the condition of the spatial integration of the transmitted light intensity by the bucket detectors, since the transmissive area of the digit "7" in T_{2IM} only occupies a part of the rectangular area of T_{1IM}, there are large nonoverlapping regions. Therefore, this mutual overlap integral value is small, and $\Delta G^{(2)}_{O1,O2}$ also satisfies the weak correlation condition required by the theoretical model.

The experimental results of the above experiments are shown in Figure 4. Panels (a) and (b) present the two-dimensional spatial distributions of the independent correlation results for object arms 1 and 2, $\Delta G^{(2)}_{R,O1}(x_R, y_R)$, and $\Delta G^{(2)}_{R,O2}(x_R, y_R)$, respectively. Panels (c)–(f) show the two-dimensional spatial distributions of the correlation results after the four fundamental arithmetic operations. Panels (g)–(j) present the one-dimensional profiles extracted along $y_R = 0$ from the distributions in (a)–(f) for quantitative analysis and comparison.

Comparing Panels (a) and (b) with (c) and (d), linear operations can fuse the two correlation images into a single correlation output. The one-dimensional profiles in Panels (g) and (h) quantitatively confirm the composition of the fused results. The spatial distribution of the experimentally measured addition correlation $\Delta G^{(2)}_{R,(O1+O2)}(x_R, 0)$ is consistent with the result obtained by directly algebraically adding the experimentally measured $\Delta G^{(2)}_{R,O1}(x_R, 0)$ and $\Delta G^{(2)}_{R,O2}(x_R, 0)$. The spatial distribution of the experimentally measured subtraction correlation $\Delta G^{(2)}_{R,(O1-O2)}(x_R, 0)$ is consistent with the result obtained by directly algebraically subtracting the experimentally measured $\Delta G^{(2)}_{R,O1}(x_R, 0)$ and $\Delta G^{(2)}_{R,O2}(x_R, 0)$. These observations are consistent with the predictions of Equation (2) for linear operations.

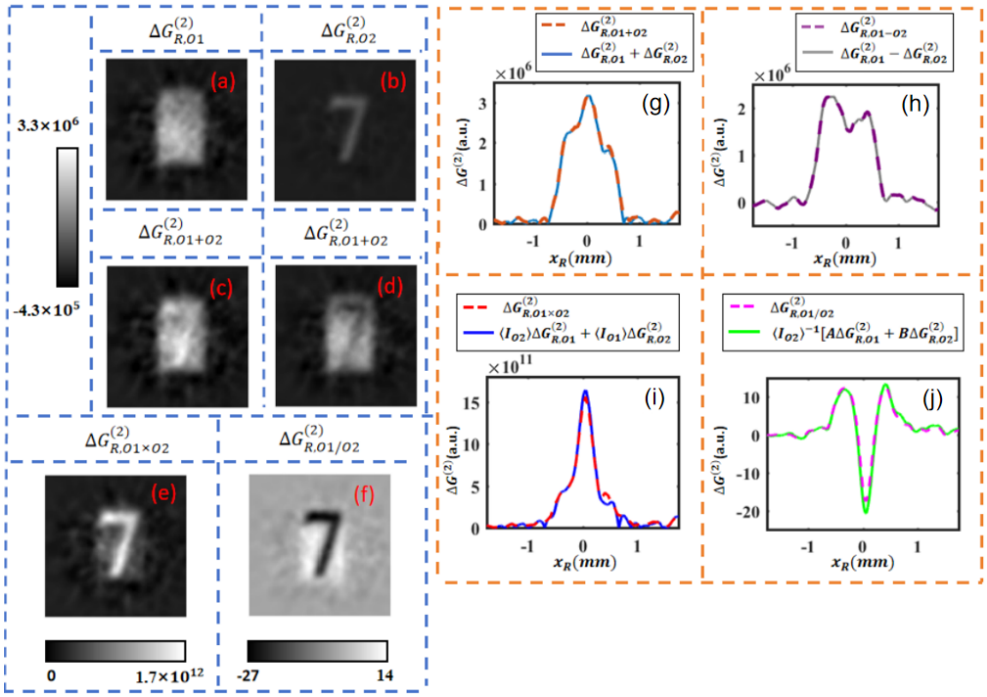


Figure 4. Theoretical and experimental results of EO-GCM under the ghost imaging configuration. (**a**,**b**) Two-dimensional spatial distributions of the intensity fluctuation correlations between the reference arm and single object beams: $\Delta G^{(2)}_{R,O1}(x_R, y_R)$ (rectangle), $\Delta G^{(2)}_{R,O2}(x_R, y_R)$ (digit "7"); (**c**–**f**) two-dimensional spatial distributions of the intensity fluctuation correlations after performing the four basic arithmetic operations on the two object beams and then correlating with the reference arm: (**c**) addition $\Delta G^{(2)}_{R,(O1+O2)}$, (**d**) subtraction $\Delta G^{(2)}_{R,(O1-O2)}$, (**e**) multiplication $\Delta G^{(2)}_{R,(O1\times O2)}$, (**f**) division $\Delta G^{(2)}_{R,(O1/O2)}$; (**g**–**j**) corresponding one-dimensional profiles extracted along $y_R = 0$ from (**a**–**f**). Solid lines: experimental measurements; dashed lines: synthetic curves calculated from the measured $\Delta G^{(2)}_{R,O1}$, $\Delta G^{(2)}_{R,O2}$, $\langle I_{O1}\rangle$, $\langle I_{O2}\rangle$, $\sigma^2_{I_{O2}}$ according to the EO-GCM theoretical formulas: linear operations correspond to algebraic addition/subtraction, multiplication corresponds to the weighted sum $\langle I_{O2}\rangle \Delta G^{(2)}_{R,O1} + \langle I_{O1}\rangle \Delta G^{(2)}_{R,O2}$, division corresponds to the weighted difference $\frac{1}{\langle I_{O2}\rangle^2}\left[A\,\Delta G^{(2)}_{R,O1} - B\,\Delta G^{(2)}_{R,O2}\right]$, where $A = \langle I_{O2}\rangle + \sigma^2_{I_{O2}}/\langle I_{O2}\rangle$, $B = \langle I_{O1}\rangle$ (denoted as A, B in the figure for brevity).

Comparing Panels (e) and (f) with (c) and (d), nonlinear operations (multiplication and division) can also fuse the two correlation images into a single correlation output, and the proportions of the "7" and rectangle are significantly different, indicating that the fused result is not ordinary algebraic addition/subtraction but a weighted form of addition/subtraction. The one-dimensional profiles in Panels (i) and (j) quantitatively confirm the composition of the fused results: the spatial distribution of the experimentally measured multiplication correlation $\Delta G^{(2)}_{R,(O1\times O2)}(x_R, 0)$ is consistent with the result calculated from the experimentally measured $\Delta G^{(2)}_{R,O1}(x_R, 0)$, $\langle I_{O1}\rangle$, $\Delta G^{(2)}_{R,O2}(x_R, 0)$, $\langle I_{O2}\rangle$ according to the weighted sum form $\langle I_{O2}\rangle \Delta G^{(2)}_{R,O1}(x_R, 0) + \langle I_{O1}\rangle \Delta G^{(2)}_{R,O2}(x_R, 0)$. The spatial distribution of the experimentally measured division correlation $\Delta G^{(2)}_{R,(O1/O2)}(x_R, 0)$ is consistent with the result calculated from the same experimental data according to the weighted difference form $\frac{1}{\langle I_{O2}\rangle^2}\left[\left(\langle I_{O2}\rangle + \frac{\sigma^2_{I_{O2}}}{\langle I_{O2}\rangle}\right)\Delta G^{(2)}_{R,O1}(x_R, 0) - \langle I_{O1}\rangle \Delta G^{(2)}_{R,O2}(x_R, 0)\right]$ (for brevity, the weighting coefficients are denoted as $A = \langle I_{O2}\rangle + \sigma^2_{I_{O2}}/\langle I_{O2}\rangle$ and $B = \langle I_{O1}\rangle$ in the figure, simplifying the weighted difference form to $\frac{1}{\langle I_{O2}\rangle^2}\left[A\,\Delta G^{(2)}_{R,O1} - B\,\Delta G^{(2)}_{R,O2}\right]$). These observations are consistent with the predictions of Equations (9) and (10) for nonlinear operations. The multiplication correlation can be expressed as a weighted sum of

two independent correlations, with the weight determined by the average intensity of the other object beam. The division correlation can be expressed as a weighted difference of two independent correlations, where the weight of the subtrahend ($\Delta G^{(2)}_{R,O1}$) is mainly proportional to the denominator path intensity $\langle I_{O2} \rangle$ and subject to a fluctuation correction inversely proportional to that intensity. The weight of the subtracted term ($\Delta G^{(2)}_{R,O2}$) is negative, with its absolute value proportional to the numerator path average intensity $\langle I_{O1} \rangle$ and inversely proportional to the square of the denominator path intensity $\langle I_{O2} \rangle^2$.

In summary, this work, through ghost interference or diffraction and ghost imaging experiments, has separately tested the descriptions of the EO-GCM theory regarding the correlation behavior of spatial frequency information and intensity distribution information in the object arm. The experimental results show that under linear operations, the correlation signal manifests as direct algebraic superposition, whereas in nonlinear operations, the intensity of one path can serve as a tuning parameter for the weight of information from the other path, thereby significantly changing the contribution proportion of each channel in the correlation result. This confirms that basic operations can be used as an effective means to manipulate information synthesis and extraction in optical correlation. To further investigate the modulation mechanism of the weight, determined by the intensity of the other path, on the correlation result in nonlinear operations (multiplication and division), we conducted further experiments based on the aforementioned ghost imaging setup (Figure 2(b1)). In the experiments, object O_{IM2} (digit "7") was kept constant, and object O_{IM1} was replaced by six O_{IM1} objects with increasing transmissive areas, as shown in Figure 5(a1–a6), placed spatially separated from the transmissive area of O_{IM2}. This arrangement aimed to make the two object arm signals satisfy the statistical independence condition. Under this condition, by adjusting the transmissive area of O_{IM1} to change the light intensity in its corresponding path, we could systematically investigate the tuning characteristics of one path's intensity on the weight of the other path's information.

Figure 5(b1–b6,c1–c6) show the two-dimensional spatial distributions of the multiplication correlation $\Delta G^{(2)}_{R,(O1\times O2)}$ and the division correlation $\Delta G^{(2)}_{R,(O1/O2)}$ under the corresponding conditions, respectively. The experimental results indicate that as $\langle I_{O1} \rangle$ increases, the contribution proportion of O_{IM2} (digit "7") in the multiplication correlation significantly increases. In the division correlation, the contribution of O_{IM2} appears as a negative value, and its magnitude increases monotonically with $\langle I_{O1} \rangle$. The two nonlinear operations achieve the linear tuning of the contribution proportion of the same information channel through positive and negative weights, respectively, and the tuning magnitude varies continuously with $\langle I_{O1} \rangle$.

To quantitatively present this evolution, Figure 5d,e show the curves of the multiplication and division correlation values at positions r_{O1} and r_{O2} as functions of $\langle I_{O1} \rangle$. Here, r_{O1} and r_{O2} are the center positions of the transmissive areas of objects O_{IM1} and O_{IM2} on the same y-axis in the relative reference frame. The experimental data show that under multiplication, the correlation values at both r_{O1} and r_{O2} are positive, and the correlation strength at r_{O2} (O_{IM2}) increases monotonically and linearly with $\langle I_{O1} \rangle$. Since the transmissive area of O_{IM2} (digit "7") remains constant, $\langle I_{O2} \rangle$ is constant, and this linear increase directly reflects the contribution of the weight factor $\langle I_{O1} \rangle$. The correlation value at r_{O1} (O_{IM1}) remains essentially constant with $\langle I_{O1} \rangle$, because $\Delta G^{(2)}_{R,O1}(r_{O1})$ characterizes the self-correlation strength at that transmissive location, which depends only on the presence of a transmissive structure at that location, not on the overall transmissive area of O_{IM1} (i.e., $\langle I_{O1} \rangle$). Under division, the correlation value at r_{O1} is positive, at r_{O2} is negative, and the absolute value of the correlation strength at r_{O2} increases monotonically with $\langle I_{O1} \rangle$ (again because $\langle I_{O2} \rangle$ is fixed, this behavior is consistent with the expectation from the weight factor $-\langle I_{O1} \rangle / \langle I_{O2} \rangle^2$). The correlation value at r_{O1} (O_{IM1}) remains essentially

constant for the same reason. This evolution trend is consistent with the expressions for nonlinear operations in the theoretical model, Equations (9) and (10).

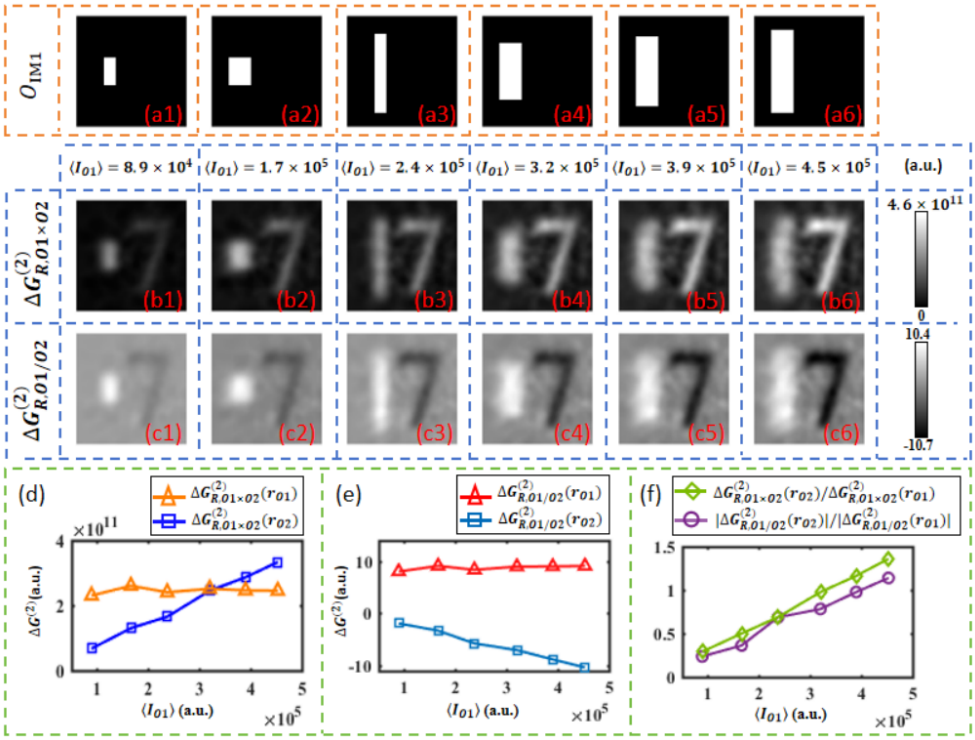


Figure 5. Experimental results of weight manipulation by nonlinear operations in EO-GCM. (**a1–a6**) Schematic diagrams of O_{IM1} objects with different transmissive areas; (**b1–b6**) two-dimensional distributions of the multiplication correlation $\Delta G^{(2)}_{R,(O1\times O2)}$ corresponding to the objects shown in (**a1–a6**); (**c1–c6**) two-dimensional distributions of the division correlation $\Delta G^{(2)}_{R,(O1/O2)}$ corresponding to the objects shown in (**a1–a6**); (**d**) curves of the multiplication correlation values at positions r_{O1}, r_{O2} on the line $y = 0$ (corresponding to the centers of the transmissive areas of O_{IM1} and O_{IM2} on the line $y = 0$) as functions of $\langle I_{O1}\rangle$; (**e**) curves of the division correlation values at the same positions as functions of $\langle I_{O1}\rangle$; (**f**) curves of the ratios $\frac{\Delta G^{(2)}_{R,(O1\times O2)}(r_{O2})}{\Delta G^{(2)}_{R,(O1\times O2)}(r_{O1})}$ and $\frac{|\Delta G^{(2)}_{R,(O1/O2)}(r_{O2})|}{|\Delta G^{(2)}_{R,(O1/O2)}(r_{O1})|}$ as functions of $\langle I_{O1}\rangle$.

Figure 5f further shows the curves of the ratios $\frac{\Delta G^{(2)}_{R,(O1\times O2)}(r_{O2})}{\Delta G^{(2)}_{R,(O1\times O2)}(r_{O1})}$ and $\frac{|\Delta G^{(2)}_{R,(O1/O2)}(r_{O2})|}{|\Delta G^{(2)}_{R,(O1/O2)}(r_{O1})|}$ as functions of $\langle I_{O1}\rangle$. The experimental data show that both ratio curves increase monotonically and linearly with $\langle I_{O1}\rangle$, and their slopes are essentially consistent on a normalized scale. This result directly verifies the conclusion that, under the condition of fixed $\langle I_{O2}\rangle$, the absolute value of the weight for the $|G^{(1)}_{R,O2}|^2$ term in division is proportional to $\langle I_{O1}\rangle$, which is completely consistent with the rule that the weight for the $|G^{(1)}_{R,O2}|^2$ term in multiplication increases linearly with $\langle I_{O1}\rangle$.

This work, through ghost interference or diffraction and ghost imaging experiments, has fully verified the correlation after arithmetic preprocessing behavior described by the EO-GCM theory and further demonstrated its application potential in information processing. The experimental results show that based on this framework, diverse operational functions such as linear fusion and separation, nonlinear weighting, and sign-adjustable processing of multichannel correlation information can be achieved. Moreover, these functions can be realized within a single imaging architecture by actively selecting the operation mode or adjusting the object arm intensities. This scheme enables continuous, predictable, all-optically controlled modulation of the contribution proportion of target features without introducing additional electro-optic modulation devices, endowing optical correlation

systems with reconfigurable information synthesis and extraction capabilities. The experimental results establish the feasibility of fundamental operations as a universal means for information manipulation in optical correlation and provide key technical support for subsequent applications in adaptive imaging, multiparameter detection, and all-optical information processing.

4. Discussion

The theoretical derivation in this paper primarily focuses on the typical case where the object arms are statistically independent ($G^{(1)}_{O1,O2} = 0$). This is because, on the one hand, this condition is easily realized in experiments, effectively suppressing the interference from inter-object mutual correlation and the three-field interference term, allowing the weight manipulation mechanism of nonlinear operations to be clearly presented. On the other hand, this case serves as a benchmark limit under general correlation conditions, providing a reasonable logical starting point for establishing the theoretical framework.

When there is a finite statistical correlation between the object arms ($G^{(1)}_{O1,O2} \neq 0$), the multiplication and division correlations described by EO-GCM explicitly depend on the first-order coherence function between the object arms. For multiplication, the inter-object mutual correlation term $\langle I_R \rangle |G^{(1)}_{O1,O2}|^2$ and the three-field interference term $2\mathrm{Re}\{G^{(1)}_{R,O1} G^{(1)*}_{R,O2} G^{(1)}_{O1,O2}\}$ in Equation (5) directly contribute to the correlation signal. For division, the influence of inter-object correlation is manifested at two levels: first, the three-field interference term $-2\mathrm{Re}\{G^{(1)}_{R,O1} G^{(1)}_{O1,O2} G^{(1)*}_{R,O2}\}/\langle I_{O2} \rangle^2$ in the first-order part of Equation (8), whose structure is completely symmetric with the multiplication case; second, the contribution $2\langle I_R \rangle |G^{(1)}_{O1,O2}|^2/\langle I_{O2} \rangle^2$ introduced in the second-order term via the Gaussian moment expansion. Notably, these two terms in division have opposite signs—the former is negative, the latter is positive—allowing the correlation signal to exhibit a continuous transition between weighted subtraction and weighted summation. This transition depends on the correlation between the object beams; in the absence of correlation, division simply reduces to a weighted subtraction.

Below, we provide a quantitative example to describe the scenario of finite inter-object correlation. Consider the ghost imaging configuration shown in Figure 2(b1), with two object masks placed as illustrated in Figure 6a,b. The two masks are identical in size but have different transmissive positions; their transmission functions along $y = 0$ are plotted in Figure 6c. Clearly, because the transmissive regions partially overlap, the two object beams are statistically correlated.

The EO-GCM simulation results are presented in Figure 6d, where panel (d1) shows the individual correlations between each object beam and the reference arm, while panels (d2) and (d3) correspond to the multiplication and division operations, respectively. It can be seen from the figure that in the non-overlapping regions, the simulation results are essentially identical to those obtained from the individually measured $\Delta G^{(2)}_{R,O1}$ and $\Delta G^{(2)}_{R,O2}$ using Equation (9). In the overlapping (statistically correlated) regions, however, discrepancies appear, which can be explained by the correlation terms in Equation (5). For the division operation, the results deviate in all three regions, because the division operation tends to approach unity in the presence of statistical correlation and is also subject to the truncation error of the Taylor expansion.

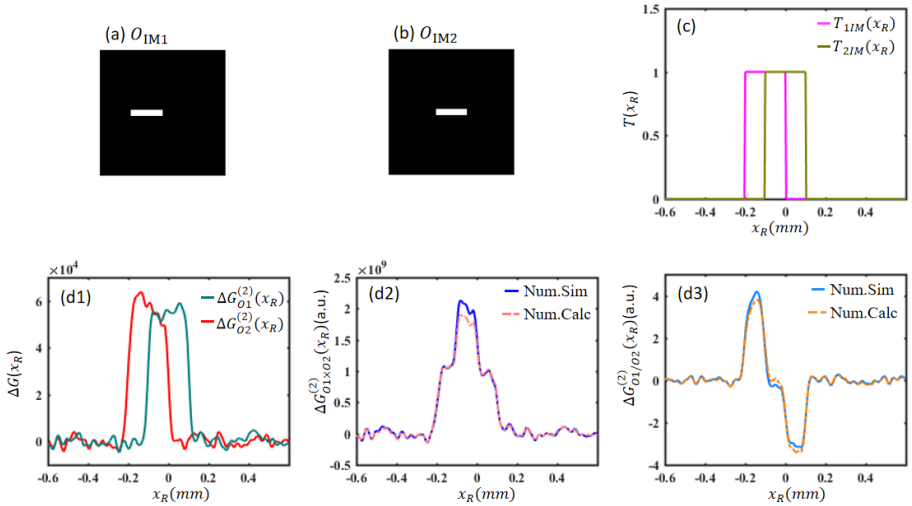


Figure 6. Numerical simulation of finite inter-object correlation. The dashed curves for multiplication and division are calculated from the numerically simulated $\Delta G^{(2)}_{R,O1}$ and $\Delta G^{(2)}_{R,O2}$ using Equations (9) and (10), respectively. (**a**,**b**) Two objects. (**c**) Transmission functions of the two objects along $y = 0$, where T_{1IM} and T_{2IM} represent the transmission functions of Object 1 and Object 2, respectively. (**d**) EO-GCM simulation results: (**d1**) individual correlations $\Delta G^{(2)}_{R,O1}$ and $\Delta G^{(2)}_{R,O2}$; (**d2**) multiplication; (**d3**) division.

It should be particularly noted that, although there is a large spatial overlap, each bucket detector integrates the total intensity from a large number M of independent speckles within the overlapping region. By the central limit theorem, the normalized second-order correlation $g^{(2)}_{O1,O2} = \langle I_{O1} I_{O2} \rangle / (\langle I_{O1} \rangle \langle I_{O2} \rangle)$ satisfies $g^{(2)}_{O1,O2} \approx 1 + 1/M$. For $M \gg 1$, this value is extremely close to unity, which means that the correlation between the total intensity fluctuations of the two object beams is very small. Therefore, even with spatial overlap, the weak-correlation assumption $\Delta G^{(2)}_{O1,O2} \approx 0$ remains a good approximation.

5. Conclusions

This study proposed the Extended Operational Ghost Correlation Model (EO-GCM) for the four fundamental arithmetic operations, systematically deriving analytical expressions for the correlation functions under addition, subtraction, multiplication, and division. The model fully retains the contributions of inter-object mutual correlation and the three-field interference term, making it applicable to arbitrary correlation scenarios. Accordingly, by considering the typical condition of weak object correlation, it clearly reveals the weight manipulation mechanism of nonlinear operations on correlation signals.

Theoretical research has reported that correlation results under linear operations strictly satisfy the superposition principle and can be directly expressed as the algebraic sum of independent correlation signals from each channel. Nonlinear operations, by coupling light intensities and their statistical fluctuations, convert the average intensity of one object path into a tuning weight for the information of the other path. Under weak correlation conditions, multiplication manifests as a weighted sum and division as a weighted difference, with the weight assignment rules being highly symmetric, except for the sign of the weight. This finding transforms nonlinear operations into a physical degree of freedom for information weighting.

Experimentally, by realizing weak object correlation conditions in both ghost interference or diffraction and ghost imaging configurations, the measurement results are in quantitative agreement with theoretical predictions. In particular, by tuning the average

intensity of one object path, the experimental system achieved continuous and linear manipulation of the contribution proportion of information from the other path and confirmed the proportionality between the absolute value of the negative weight in division and the average intensity of the numerator path. These results provide direct experimental evidence for signal processing functions, such as selective extraction of multi-channel information, dynamic weighting, and sign-adjustable processing.

EO-GCM provides a systematic mathematical description and experimental validation for basic operations on multipath object arm signals in optical correlation, enabling ghost imaging systems to achieve reconfigurable, weighted correlation fusion-based continuous modulation of target features within a single architecture. This work lays the theoretical and technical foundation for fields such as adaptive imaging, multiparameter detection, and all-optical information processing.

Author Contributions: Conceptualization, J.Z. and H.W.; methodology, J.Z.; software, J.Z.; validation, J.Z. and H.W.; formal analysis, J.Z.; investigation, J.Z.; data curation, J.Z.; writing—original draft preparation, J.Z.; writing—review and editing, J.Z. and H.W.; visualization, J.Z.; supervision, H.W.; project administration, H.W.; funding acquisition, H.W. All authors have read and agreed to the published version of the manuscript.

Funding: National Natural Science Foundation of China (No. 61675028) and the Fundamental Research Funds for the Central Universities.

Institutional Review Board Statement: Not applicable.

Informed Consent Statement: Not applicable.

Data Availability Statement: The datasets presented in this article are not readily available because the data are part of an ongoing study.

Acknowledgments: All authors have read and agreed to the published version of the manuscript.

Conflicts of Interest: The authors declare no conflicts of interest. The funders had no role in the design of the study; in the collection, analyses, or interpretation of data; in the writing of the manuscript, or in the decision to publish the results.

References

1. Hanbury Brown, R.; Twiss, R.Q. A test of a new type of stellar interferometer on Sirius. *Nature* **1956**, *178*, 1046–1048. [CrossRef]
2. Glauber, R.J. The quantum theory of optical coherence. *Phys. Rev.* **1963**, *130*, 2529–2539. [CrossRef]
3. Strekalov, D.V.; Sergienko, A.V.; Klyshko, D.N.; Shih, Y.H. Observation of two-photon "ghost" interference and diffraction. *Phys. Rev. Lett.* **1995**, *74*, 3600–3603. [CrossRef] [PubMed]
4. Pittman, T.B.; Shih, Y.H.; Strekalov, D.V.; Sergienko, A.V. Optical imaging by means of two-photon quantum entanglement. *Phys. Rev. A* **1995**, *52*, R3429–R3432. [CrossRef] [PubMed]
5. Bennink, R.S.; Bentley, S.J.; Boyd, R.W. Two-photon coincidence imaging with a classical source. *Phys. Rev. Lett.* **2002**, *89*, 113601. [CrossRef] [PubMed]
6. Bennink, R.S.; Bentley, S.J.; Boyd, R.W.; Howell, J.C. Quantum and classical coincidence imaging. *Phys. Rev. Lett.* **2004**, *92*, 033601. [CrossRef]
7. Cheng, J.; Han, S. Incoherent coincidence imaging and its applicability in X-ray diffraction. *Phys. Rev. Lett.* **2004**, *92*, 093903. [CrossRef]
8. Ferri, F.; Magatti, D.; Gatti, A.; Bache, M.; Brambilla, E.; Lugiato, L.A. High-resolution ghost image and ghost diffraction experiments with thermal light. *Phys. Rev. Lett.* **2005**, *94*, 183602. [CrossRef]
9. Gatti, A.; Brambilla, E.; Bache, M.; Lugiato, L.A. Ghost imaging with thermal light: Comparing entanglement and classical correlation. *Phys. Rev. Lett.* **2004**, *93*, 093602. [CrossRef]
10. Valencia, A.; Scarcelli, G.; D'Angelo, M.; Shih, Y. Two-photon imaging with thermal light. *Phys. Rev. Lett.* **2005**, *94*, 063601. [CrossRef]
11. Zhang, D.; Zhai, Y.-H.; Wu, L.-A.; Chen, X.-H. Correlated two-photon imaging with true thermal light. *Opt. Lett.* **2005**, *30*, 2354–2356. [CrossRef]
12. Cai, Y.; Zhu, S.-Y. Ghost interference with partially coherent radiation. *Opt. Lett.* **2004**, *29*, 2716–2718. [CrossRef]

13. Wang, K.; Cao, D.-Z. Subwavelength coincidence interference with classical thermal light. *Phys. Rev. A* **2004**, *70*, 041801(R). [CrossRef]
14. Xiong, J.; Cao, D.-Z.; Huang, F.; Li, H.-G.; Sun, X.-J.; Wang, K. Experimental observation of classical subwavelength interference with a pseudothermal light source. *Phys. Rev. Lett.* **2005**, *94*, 173601. [CrossRef]
15. Li, P.-M.; Chen, X.-J.; Qiu, X.-D.; Chen, B.-L.; Chen, L.-X.; Sun, B.-Q. Ghost imaging, development, and recent advances. *Chin. Opt. Lett.* **2024**, *22*, 112701. [CrossRef]
16. Han, S.; Yu, H.; Shen, X.; Liu, H.; Gong, W.; Liu, Z. A review of ghost imaging via sparsity constraints. *Appl. Sci.* **2018**, *8*, 1379. [CrossRef]
17. Liu, B.; Wang, F.; Chen, C.; Dong, F.; McGloin, D. Self-evolving ghost imaging. *Optica* **2021**, *8*, 1340–1349. [CrossRef]
18. Qiu, X.; Zhang, D.; Ma, T.; Lin, F.; Guo, H.; Zhang, W.; Chen, L. Parallel ghost imaging. *Adv. Quantum Technol.* **2020**, *3*, 2000073. [CrossRef]
19. Qiu, X.; Guo, H.; Chen, L. Remote transport of high-dimensional orbital angular momentum states and ghost images via spatial-mode-engineered frequency conversion. *Nat. Commun.* **2023**, *14*, 8244. [CrossRef]
20. Ye, Z.; Hou, W.; Ding, C.X.; Men, X.J.; He, R.J.; Zhao, J.; Wang, H.B.; Xiong, J.; Wang, K. Random Holography: Generating EPR-Like Correlation with Thermal Photons. *Laser Photonics Rev.* **2025**, *19*, 2401610. [CrossRef]
21. Hou, W.; He, R.J.; Ye, Z.; Men, X.J.; Ding, C.X.; Liu, H.C.; Wang, H.B.; Xiong, J. Manipulating classical triple correlations for optical information processing and metrology. *Photonics Res.* **2025**, *13*, 2073–2087. [CrossRef]
22. Du, L.K.; Hu, C.; Nie, Z.W.; Chang, C.; Sun, S.; Liu, S.; Deng, C.; Bo, Z.; Liu, W.T.; Han, S. Information-quantitative evaluation of linear computational imaging and application in ghost imaging. *Opt. Laser Technol.* **2025**, *192*, 113893. [CrossRef]
23. Gatti, A.; Brambilla, E.; Bache, M.; Lugiato, L.A. Correlated imaging, quantum and classical. *Phys. Rev. A* **2004**, *70*, 013802. [CrossRef]
24. Meyers, R.E.; Deacon, K.S.; Shih, Y. Turbulence-free ghost imaging. *Appl. Phys. Lett.* **2011**, *98*, 111115. [CrossRef]
25. Meyers, R.E.; Deacon, K.S.; Shih, Y. Positive–negative turbulence-free ghost imaging. *Appl. Phys. Lett.* **2012**, *100*, 131114. [CrossRef]
26. Sun, S.; Nie, Z.-W.; Xu, Y.-K.; Chang, C.; Chen, P.-X.; Lai, P.-X.; Liu, W.-T. Quantum-inspired computational wavefront shaping enables turbulence-resilient distributed aperture synthesis imaging. *Sci. Adv.* **2025**, *11*, eaea4152. [CrossRef]
27. He, R.-J.; Ye, Z.; Liu, H.-C.; Wang, H.-B.; Xiong, J. Label-free correlation adaptive optics using even-symmetrical thermal light. *APL Photonics* **2025**, *10*, 12. [CrossRef]
28. Lin, F.; Hong, L.; Guo, H.; Qiu, X.; Chen, L. Ghost identification for QR codes and fingerprints with thermal light modulation. *Phys. Rev. Appl.* **2022**, *18*, 054060. [CrossRef]
29. Ye, Z.; Zhou, C.; Ding, C.-X.; Zhao, J.; Jiao, S.; Wang, H.-B.; Xiong, J. Ghost diffractive deep neural networks: Optical classifications using light's second-order coherence. *Phys. Rev. Appl.* **2023**, *20*, 054012. [CrossRef]
30. Ma, Y.; Wang, X.; Wang, L.; Zhao, S.; Han, S. Parallel computational ghost imaging with modulation patterns multiplexing and permutation inspired by compound eyes. *Appl. Phys. Lett.* **2024**, *124*, 081105. [CrossRef]
31. Wang, X.; Ma, Y.; Wang, L.; Zhao, S.; Han, S. Multi-channel computational ghost imaging based on multi-scale speckle optimization. *J. Opt.* **2024**, *26*, 025703. [CrossRef]
32. Liu, X.-F.; Shi, J.-H.; Wu, X.-Y.; Zhai, G.-J. Multi-Path Ghost Imaging by Means of an Additional Time Correlation. *Chin. Phys. Lett.* **2019**, *36*, 024203. [CrossRef]
33. Chen, Z.; Yu, J.; Lin, F.; Chen, L. Image matching based on third-order correlation ghost imaging. *Phys. Rev. Appl.* **2026**, *25*, 014019. [CrossRef]
34. Moodley, C.; Forbes, A. Advances in Quantum Imaging with Machine Intelligence. *Laser Photonics Rev.* **2024**, *18*, 2300939. [CrossRef]
35. Abbas, A.; Mu, J.; Mengyue, Z.; Cao, J.; Zhang, X. Target recognition in ghost imaging from traditional to advance; a brief review. *Opt. Laser Technol.* **2025**, *184*, 112478. [CrossRef]
36. Tao, R.; Wang, C.; Chen, Z.; Xue, X. Deep learning-enhanced spectral ghost imaging with accelerated and high-fidelity reconstruction. *Appl. Opt.* **2025**, *64*, 7799–7806. [CrossRef]
37. Oh, S.; Tian, T.; Sun, Z.; Spielmann, C. Efficient high-resolution microscopic ghost imaging via sequenced speckle illumination and deep learning from a single noisy image. *Adv. Opt. Technol.* **2025**, *14*, 1583836. [CrossRef]
38. Wang, Y.; Gao, C.; Wang, X.-Q.; Yao, Z.-H. Self-supervised deep learning ghost imaging through scattering media based on dual physical models. *Eur. Phys. J. Plus* **2025**, *140*, 701. [CrossRef]
39. Zhou, C.; Cao, J.; Yao, H.; Cui, H.; Zhang, H.; Hao, Q. Enhanced ghost imaging reconstruction via a Chambolle-Pock inspired deep unfolding network. *Opt. Laser Technol.* **2025**, *191*, 113323. [CrossRef]
40. Wang, Y.; Gao, C.; Wang, X.-Q.; Yao, Z.-H. The ghost imaging method based on dual attention mechanism and orthogonal optimization. *Phys. Scr.* **2025**, *100*, 095007. [CrossRef]

41. Zhang, T.; Peng, Y.; Chen, W. High-quality ghost imaging through highly complex scattering media with physics-enhanced untrained neural networks. *Opt. Express* **2025**, *33*, 34346–34357. [CrossRef]
42. Goodman, J.W. *Statistical Optics*, 2nd ed.; Wiley: New York, NY, USA, 2015.
43. Liu, H.-C.; Yang, H.; Xiong, J.; Zhang, S. Positive and negative ghost imaging. *Phys. Rev. Appl.* **2019**, *12*, 034019. [CrossRef]
44. Bai, Y.; Han, S. Ghost imaging with thermal light by third-order correlation. *Phys. Rev. A* **2007**, *76*, 043828. [CrossRef]
45. Ou, L.-H.; Kuang, L.-M. Ghost imaging with third-order correlated thermal light. *J. Phys. B At. Mol. Opt. Phys.* **2007**, *40*, 1833–1844. [CrossRef]
46. Liu, H.; Wang, K. On Ghost Imaging Studies for Information Optical Imaging. *Appl. Sci.* **2022**, *12*, 10981. [CrossRef]
47. Tian, T.; Li, W.; Zhang, J. Multi-wavelength ghost imaging: A review. *Vicinagearth* **2025**, *2*, 4. [CrossRef]
48. Gong, W.; Han, S. Ghost imaging Lidar: Principle, progress and prospect. *J. Opt.* **2024**, *26*, 123001. [CrossRef]

Disclaimer/Publisher's Note: The statements, opinions and data contained in all publications are solely those of the individual author(s) and contributor(s) and not of MDPI and/or the editor(s). MDPI and/or the editor(s) disclaim responsibility for any injury to people or property resulting from any ideas, methods, instructions or products referred to in the content.